

## Magnetic Properties

## Spectroscopic Studies of the Magnetic Excitation and Spin-Phonon Couplings in a Single-Molecule Magnet

Shelby E. Stavretis,<sup>[a]</sup> Duncan H. Moseley,<sup>[a]</sup> Fan Fei,<sup>[b]</sup> Hui-Hui Cui,<sup>[b]</sup> Yongqiang Cheng,<sup>\*,[c]</sup> Andrey A. Podlesnyak,<sup>\*,[c]</sup> Xiaoping Wang,<sup>\*,[c]</sup> Luke L. Daemen,<sup>[c]</sup> Christina M. Hoffmann,<sup>[c]</sup> Mykhaylo Ozerov,<sup>\*,[d]</sup> Zhengguang Lu,<sup>[d]</sup> Komalavalli Thirunavukkuarasu,<sup>[e]</sup> Dmitry Smirnov,<sup>[d]</sup> Tiejian Chang,<sup>[f]</sup> Yu-Sheng Chen,<sup>[f]</sup> Anibal J. Ramirez-Cuesta,<sup>[c]</sup> Xue-Tai Chen,<sup>[b]</sup> and Zi-Ling (Ben) Xue<sup>\*,[a]</sup>

**Abstract:** Large separations between ground and excited magnetic states in single-molecule magnets (SMMs) are desirable to reduce the likelihood of spin reversal in the molecules. Spin-phonon coupling is a process leading to magnetic relaxation. Both the reversal and coupling, making SMMs lose magnetic moments, are undesirable. However, direct determination of large magnetic states separations ( $> 45 \text{ cm}^{-1}$ ) is challenging, and few detailed investigations of the spin-phonon coupling have been conducted. The magnetic separation in  $[\text{Co}(\text{12-crown-4})_2](\text{I}_3)_2(\text{12-crown-4})$  (**1**) is

determined and its spin-phonon coupling is probed by inelastic neutron scattering (INS) and far-IR spectroscopy. INS, using oriented single crystals, shows a magnetic transition at  $49.4(1.0) \text{ cm}^{-1}$ . Far-IR reveals that the magnetic transition and nearby phonons are coupled, a rarely observed phenomenon, with spin-phonon coupling constants of  $1.7\text{--}2.5 \text{ cm}^{-1}$ . The current work spectroscopically determines the ground–excited magnetic states separation in an SMM and quantifies its spin-phonon coupling, shedding light on the process causing magnetic relaxation.

## Introduction

Transition-metal complexes showing slow magnetic relaxation have been actively studied for possible use as single-molecule magnets (SMMs) and chemical qubits.<sup>[1]</sup> One type of such complexes are paramagnetic compounds with  $S \geq 1$  and quenched orbital angular momenta. This leads to magnetic anisotropy and zero-field splitting (ZFS) of the ground electronic states of the compounds.<sup>[1a–q]</sup> Axial ( $D$ ) and rhombic ( $E$ ) ZFS parameters are possible measures of the magnetic anisotropy. For example, the ZFS diagram of  $[\text{Co}(\text{12C4})_2](\text{I}_3)_2(\text{12C4})$  (**1**,  $S = 3/2$ ;  $12\text{C4} = 12\text{-crown-4}$ ), the first eight-coordinate mononuclear SMM with axial anisotropy ( $D < 0$ ),<sup>[2]</sup> for a local  $D_{4d}$  field is shown in Figure 1. When  $D < 0$ , as in **1**, the molecule has an

easy axis of magnetization in the  $z$  direction, which is typically parallel to the pseudo or actual highest symmetry axis. When  $D > 0$ , the molecule possesses an easy plane of magnetization in the  $x, y$  direction. The determination of the ZFS parameters is vital to understanding magnetic properties of SMMs.<sup>[1a–q]</sup>

Magnetometry has been widely employed to estimate the ZFS in SMMs.<sup>[1d]</sup> However, it often leads to an equivocal determination of the ZFS, as magnetometry is essentially a multi-parameter fit of susceptibility and magnetization data by using the spin-Hamiltonian. Also, the sign of  $D$  is often not accurately determined. Spectroscopic techniques, such as high-frequency and high-field electron paramagnetic resonance (HF-EPR), are powerful tools to study SMMs with ZFS up to approximately  $33 \text{ cm}^{-1}$  (1 THz).<sup>[1d,2a]</sup> Far-IR magneto spectroscopy (FIRMS) is a

[a] S. E. Stavretis, D. H. Moseley, Prof. Z.-L. Xue  
Department of Chemistry, University of Tennessee  
Knoxville, Tennessee 37996 (USA)  
E-mail: xue@utk.edu

[b] F. Fei, H.-H. Cui, Prof. X.-T. Chen  
State Key Laboratory of Coordination Chemistry  
School of Chemistry and Chemical Engineering  
Nanjing University, Nanjing 210023 (China)

[c] Dr. Y. Cheng, Dr. A. A. Podlesnyak, Dr. X. Wang, Dr. L. L. Daemen,  
Dr. C. M. Hoffmann, Dr. A. J. Ramirez-Cuesta  
Neutron Scattering Division, Oak Ridge National Laboratory  
Oak Ridge, Tennessee 37831 (USA)  
E-mail: chengy@ornl.gov  
podlesnyakaa@ornl.gov  
wangx@ornl.gov

[d] Dr. M. Ozerov, Z. Lu, Dr. D. Smirnov  
National High Magnetic Field Laboratory  
Tallahassee, Florida 32310 (USA)  
E-mail: ozerov@magnet.fsu.edu

[e] Prof. K. Thirunavukkuarasu  
Department of Physics, Florida A&M University  
Tallahassee, Florida 32307 (USA)

[f] T. Chang, Dr. Y.-S. Chen  
ChemMatCARS, Center for Advanced Radiation Sources  
The University of Chicago, Argonne, Illinois 60439 (USA)

 Supporting information including author contributions and the ORCID identification number(s) for the author(s) of this article can be found under:  
<https://doi.org/10.1002/chem.201903635>.

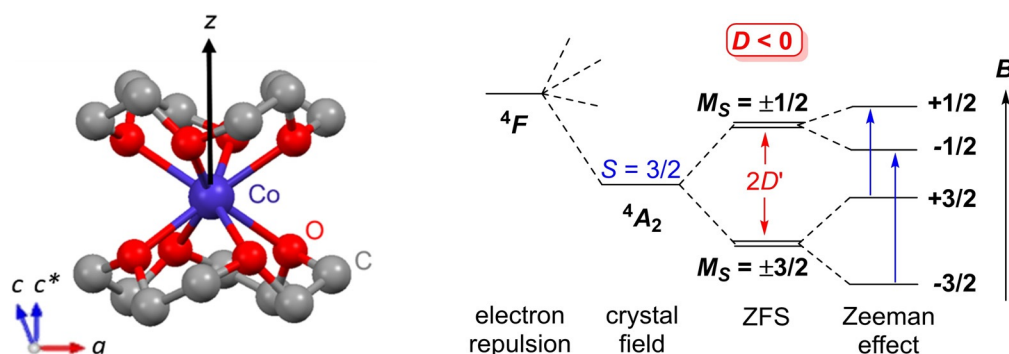


**Figure 1.** Left: Cation in **1** showing the molecular  $z$  axis indicated by the black arrow. H atoms are omitted for clarity. The local symmetry around the  $\text{Co}^{\text{II}}$  ion is close to  $D_{4d}$ . Right: Ground-state quartet levels in high-spin,  $d^7$  complexes with  $D_{4d}$  symmetry. When  $E=0$ ,  $D'=(D^2+3E^2)^{1/2}$ . Under magnetic fields, the Kramers doublets split based on the Zeeman effect, leading to the presence of the  $M_S = -3/2 \rightarrow -1/2$  and  $M_S = +3/2 \rightarrow +1/2$  transitions at low temperatures.

direct technique to probe transitions between the ZFS states in transition-metal complexes and magnetic transitions in f-element complexes.<sup>[1d,3]</sup> Brackett et al. showed that transitions between the ZFS states are magnetic-dipole allowed and thus observable by far-IR spectroscopy.<sup>[4]</sup> In FIRMS, the sample is placed in variable magnetic fields while its far-IR spectra are collected. The Zeeman effect on the magnetic levels helps reveal magnetic transitions when they overlap with phonon peaks. FIRMS is generally employed to probe magnetic excitations in SMMs that are unreachable by HF-EPR. Inelastic neutron scattering (INS) is another unique, direct probe<sup>[5]</sup> to study magnetic excitations in complexes of both  $d^{6i}$  and  $f$  metals.<sup>[7]</sup> The prevalence of phonons in the region above  $20\text{ cm}^{-1}$  creates a particular challenge when studying magnetic transitions in metal complexes. Temperature dependence and diamagnetic controls have been utilized to distinguish magnetic excitations from phonons in INS.<sup>[6m,7a]</sup> As magnetic and phonon peaks exhibit different temperature dependences, the Bose correction has been used to reveal the magnetic excitation in INS spectra.<sup>[6i,m]</sup> However, the use of diamagnetic controls and temperature dependence to probe magnetic excitations by INS is not always successful when the expected magnetic contribution is weak and the background contributions of H atoms are strong.<sup>[8]</sup> One essentially unexplored area is conducting INS with applied magnetic fields to distinguish magnetic peaks from phonons. Magnetic transitions would be subjected to the Zeeman effect and therefore shift in energy with field, whereas phonons for the most part remain unchanged. To our knowledge, no conclusive measurements of inter-Kramers doublet (KD) transitions in mononuclear transition-metal complexes by magneto-INS have been reported.<sup>[6b,m,9]</sup>

Spin-phonon coupling in SMMs has been studied as a mechanism for spin relaxation.<sup>[1a-d]</sup> Rechkemmer et al. have observed two field-dependent peaks by FIRMS in a  $\text{Co}^{\text{II}}$  complex (idealized  $D_{2d}$  symmetry), which they attributed to spin-phonon coupling.<sup>[3c]</sup> We have recently reported distinct couplings of  $g$  phonons with the magnetic ZFS transition in the SMM  $\text{Co}(\text{acac})_2(\text{H}_2\text{O})_2$  ( $C_{2h}$  symmetry) and its isotopologues as avoided crossings in Raman spectroscopy with coupling constants of  $1\text{--}2\text{ cm}^{-1}$ .<sup>[10]</sup> In contrast, no spin-phonon coupling with the IR-active phonons was observed in  $\text{Co}(\text{acac})_2(\text{H}_2\text{O})_2$ .<sup>[10]</sup> The nature

of spin-phonon couplings in molecular complexes is still not well understood. Other than  $\text{Co}(\text{acac})_2(\text{H}_2\text{O})_2$  and its isotopologues,<sup>[10]</sup> there has been no report on the magnitude of the couplings.<sup>[3f]</sup> Theoretical studies have been performed recently to understand the interactions between electron spins and phonons, leading to relaxation in SMMs.<sup>[11]</sup>

In this work, we have employed INS and FIRMS to study the magnetic inter-Kramers excitation  $M_S = \pm 3/2 \rightarrow \pm 1/2$  in **1**, the first eight-coordinate mononuclear SMM with axial anisotropy ( $D < 0$ ).<sup>[2]</sup> One particular challenge in the study of **1** by INS is that each molecule of **1** has a large incoherent neutron scattering background from 48H atoms of  $[\text{Co}(\text{12C4})_2](\text{I}_3)_2$  and free 12C4 in the crystal lattice.<sup>[12]</sup> In addition, distinct spin-phonon couplings between IR-active phonons and the  $M_S = -3/2 \rightarrow -1/2$  transition as avoided crossings have been probed by FIRMS. Our spectroscopic studies of **1** are reported here.

## Results and Discussion

For molecular compound **1**, phonons refer to both external (intermolecular) and internal (intramolecular) vibrational modes in the solid. Internal modes are molecular vibrations, in which the molecules maintain almost no displacement of the mass center.<sup>[13]</sup> External modes are lattice vibrations, when molecules vibrate primarily as a whole with little internal distortion, and include translational and librational modes with much lower frequencies than internal modes.<sup>[5a]</sup> Internal and external modes often couple as they originate from the same governing equations.<sup>[5a,13]</sup> Thus, we do not distinguish external and internal modes in the current work and refer to all vibrations as phonons.

The structure of the cation in **1**,  $[\text{Co}(\text{12C4})_2]^{2+}$ , is shown in Figure 1, left. The molecular  $z$  axis (Figure 1), which is along the  $C_4$  axis, is pointed nearly along the crystallographic reciprocal  $c^*$  axis. The ZFS diagram for this  $S=3/2$ ,  $D < 0$  system under the perturbation of the local  $D_{4d}$  field is shown in Figure 1, right. Earlier field-dependent magnetization studies and computations by others using the CASPT2 method gave  $D = -38.0\text{ cm}^{-1}$ ,  $E = -0.75\text{ cm}^{-1}$  and  $D = -70.1\text{ cm}^{-1}$ ,  $E = 1.05\text{ cm}^{-1}$ , respectively.<sup>[2]</sup> The spin-Hamiltonian for such an  $S =$

3/2 system with ZFS and Zeeman effect is given in Equation (1):

$$\hat{H}_S = D(\hat{S}_z^2 - 5/4) + E(\hat{S}_x^2 - \hat{S}_y^2) + \mu_B g_x B_x \hat{S}_x + \mu_B g_y B_y \hat{S}_y + \mu_B g_z B_z \hat{S}_z \quad (1)$$

where  $\hat{S}$  = spin operator,  $\mu_B$  = electron Bohr magneton,  $g$  =  $g$ -factor,  $B$  = applied magnetic field.

### Single-crystal X-ray and neutron diffraction studies

The single-crystal diffraction studies have confirmed that there is no phase change between 293 K and 10.15 K, and determined the orientation of two large crystals of **1** used for subsequent INS studies. Previously, the structure of **1** was determined at 293 K by single-crystal X-ray diffraction.<sup>[14]</sup> As the current spectroscopic and earlier magnetometry measurements were performed at low temperatures, it is important to know what the structure of **1** is at 10.15 K. X-ray diffraction at the Argonne National Laboratory (ANL) shows that the structure of **1** at 10.15 K is essentially the same as that at 293 K, although the cell volume decreases by 3.68% (ca.  $0.5 \text{ \AA}^{-3} \text{ K}^{-1}$ ).<sup>[14]</sup> Single-crystal neutron diffraction studies were performed at 100 K by using TOPAZ, a single-crystal neutron diffractometer at the Spallation Neutron Source (SNS), Oak Ridge National Laboratory (ORNL). ORTEP diagrams of the two structures are given in Figure S3. Crystallographic parameters and selected bond lengths and angles are given in Table S1 with comparison with the structure at 293 K.

The orientation of the two large single crystals ( $8 \times 3.25 \times 2 \text{ mm}^3$ , 100.1 mg and  $8 \times 2.75 \times 1 \text{ mm}^3$ , 80.0 mg; photos of the crystals in Figure S1) of **1** used in the INS studies were also determined by using TOPAZ.<sup>[5b,15]</sup> Large single crystals are desirable for INS studies inside magnetic fields. These crystals are well beyond the X-ray beam size. In addition, such large crystals would have significant X-ray absorption in diffraction experiments, affecting measured diffraction intensities and causing errors in the structure determined by X-ray diffraction. Thus, neutron diffraction of **1** was conducted as TOPAZ was capable of handling such large crystals.<sup>[5b,15]</sup>

### INS studies of **1**

In neutron scattering processes, the incident neutrons penetrate a sample and are scattered from interactions with either atomic nuclei or unpaired electrons in the sample.<sup>[5b,12,16]</sup> The scattering by unpaired electrons is from the magnetic interactions between neutron spins and electron spins, and is called magnetic scattering.

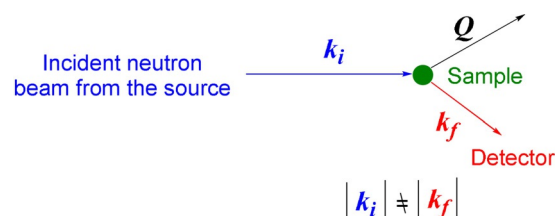
The magnetic scattering cross section in neutron scattering corresponds to the number of neutrons scattered per second owing to the magnetic interaction into a solid angle  $d\Omega$  with energy transfer between  $\eta\omega$  and  $\eta(\omega + d\omega)$  divided by the flux of the incident neutrons. If unpolarized neutrons are scattered from identical magnetic ions with localized electrons, the magnetic scattering cross section for spin-only scattering is expressed by Equation (2).<sup>[12,17]</sup>

$$\frac{d^2\sigma}{d\Omega d\omega} = (\gamma r_0)^2 \frac{k_f}{k_i} \left[ \frac{1}{2} g F(\mathbf{Q})^2 e^{-2W(\mathbf{Q})} \sum_{\alpha,\beta} \left( \delta_{\alpha\beta} - \frac{Q_\alpha \cdot Q_\beta}{Q^2} \right) S^{\alpha\beta}(\mathbf{Q}, \omega) \right] \quad (2)$$

where  $\sigma$  = neutron cross section;  $\gamma$  = gyromagnetic ratio;  $r_0$  = classical radius of an electron;  $g$  = Landé  $g$ -factor;  $F(\mathbf{Q})$  = dimensionless magnetic form factor defined as the Fourier transform of the normalized spin density associated with magnetic ions;  $e^{-2W(\mathbf{Q})}$  = Debye–Waller factor caused by thermal motion;  $S^{\alpha\beta}(\mathbf{Q}, \omega)$  = magnetic scattering function;  $\left( \delta_{\alpha\beta} - \frac{Q_\alpha \cdot Q_\beta}{Q^2} \right)$  = polarization factor, which implies neutrons can only couple to magnetic moments or spin fluctuations perpendicular to  $\mathbf{Q}$ ;  $\eta\omega$  = energy change experienced by the sample;  $\omega$  = angular frequency of the neutron;  $\mathbf{Q}$  is defined below.

In the scattering processes, some scattered neutrons do not change energy but simply change their direction in a process called elastic neutron scattering. Elastic neutron scattering is the basic process in neutron crystal diffraction discussed earlier. In addition to the elastic scattering, other neutrons transfer energies with the sample during the scattering process, leading to changes of both their direction and energy. This process is called inelastic neutron scattering (INS). Both elastic and inelastic neutron scattering occur at the same time during interaction with the sample.

The INS process is represented in Scheme 1 using incident neutrons (with momentum  $k_i$ ). The neutron is scattered by the sample, giving a final neutron momentum  $k_f$  and the momentum transfer,  $\mathbf{Q} = k_i - k_f$ . INS is a unique method to distinguish magnetic peaks from phonons. Peaks of magnetic excitations decrease in intensity with increased  $|\mathbf{Q}|$ ,<sup>[5b,12,16]</sup> whereas phonons increase in intensity with increased  $|\mathbf{Q}|$ .



**Scheme 1.** Schematic of the inelastic neutron scattering (INS) processes.  $k_i$  and  $k_f$  are the momenta of the incoming and outgoing neutrons, respectively.  $\mathbf{Q} = k_i - k_f$  is the momentum transfer.

Two types of INS instruments, direct-geometry and indirect-geometry time-of-flight (TOF) spectrometers, have been used in the current work. The features of both types and their use for coordination chemistry research have been reviewed.<sup>[5b]</sup> In a direct-geometry spectrometer, the selected incident energy  $E_i$  is fixed (monochromatic) and  $E_f$  is measured by TOF to determine the energy transfer ( $E_i - E_f$ ).<sup>[12]</sup> allowing for a wide range of  $\mathbf{Q}$  measurements. The Cold Neutron Chopper Spectrometer (CNCS at SNS, ORNL) in the current work is a direct-geometry instrument.<sup>[5,18]</sup> In the indirect-geometry INS spectrometers, the final energy,  $E_f$ , of the scattered neutrons reaching the detec-

tors is fixed. The incident neutrons here can be a “white” beam (with a range of energies) where  $E_i$  is determined through TOF, giving a wide energy transfer up to, for example, approximately  $4000\text{ cm}^{-1}$  with high energy/spectral resolution for the Vibrational Spectrometer (VISION at SNS), which was used in the current work.<sup>[19]</sup> Indirect-geometry INS spectrometers give phonons (in particular molecular vibrations of chemical compounds) with no selection rules that govern IR and Raman spectroscopies.<sup>[5]</sup> However,  $Q$  information is limited in indirect-geometry spectrometers.

Complex **1** was studied under variable magnetic fields by CNCS using the two large crystals of **1** indicated earlier. Neutron flux is usually much smaller than photon flux used in spectroscopy, leading to low signals in INS.<sup>[12]</sup> Thus, larger samples/crystals likely enhance the INS signals. The two crystals were tiled together and aligned with their  $c^*$  axes parallel to the magnetic field (Figure S2). The crystallographic  $c^*$  axes had been determined at the single-crystal neutron diffractometer TOPAZ. This places the magnetic field  $B_z$  of the instrument (CNCS) parallel to the molecular  $z$  axis. This alignment should give orientation-dependent splitting in the  $B_z$  direction. The use of the large single crystals with predetermined orientations significantly improves the data quality by reducing the broadening of the magnetic peak observed in powder samples caused by the random orientation of the molecules inside magnetic fields ( $B_z, B_x, B_y$ ). With an applied magnetic field, the  $M_S = -3/2 \rightarrow -1/2$  transition in **1** at 2.0 K was probed with an incident neutron energy of  $97.34\text{ cm}^{-1}$ . The spectra at 0, 2, 5,

and 8 T are shown in Figure 2, with an expanded view of the spectra and waterfall plots in Figure S4. The magnetic peak  $2D'$  at 0 T is evident at  $49.4(1.0)\text{ cm}^{-1}$ . A contour plot in the INS spectra showing the shift of the  $2D'$  peak is given in Figure 2B (although it appears as a series of discrete increases owing to the low number of fields measured). This blueshift of the magnetic peak is consistent with the  $M_S = -3/2 \rightarrow -1/2$  transition in single crystals aligned in the  $z$  direction. The small remaining peak at  $49.4\text{ cm}^{-1}$  at 8 T is an overlapping phonon mode that does not show a noticeable energy shift with the field, and it is possibly the No. 23 phonon in Table S2. The ZFS mode eventually overlaps with another peak at approximately  $58\text{ cm}^{-1}$  (phonons Nos. 24–28 in Table S2) at 8 T. There is no observable redshift in intensity in the INS representing the  $M_S = +3/2 \rightarrow +1/2$  transition (Figure 1, right), possibly because at 2 K, there are few molecules at the excited  $M_S = +3/2$  state, and most molecules are at the ground  $M_S = -3/2$  state. In the plot of the peak intensities versus  $|Q|$  collected at CNCS in Figure 2C, the peak at  $49.4(1.0)\text{ cm}^{-1}$  gradually loses intensity with increasing  $|Q|$ , supporting its assignment as the magnetic (ZFS) peak as peaks of magnetic origin have stronger intensity at lower  $|Q|$ .<sup>[5b]</sup> In contrast, phonons tend to show stronger intensity at higher  $|Q|$ . To our knowledge, the current work is the first example of studying single crystals of a transition-metal complex by INS inside magnetic fields.<sup>[6–7]</sup>

Variable-temperature INS of **1** at 10–125 K were collected with the Vibrational Spectrometer (VISION)<sup>[5b,19]</sup> at zero field. VISION has a relatively large signal/noise ratio for an INS instru-

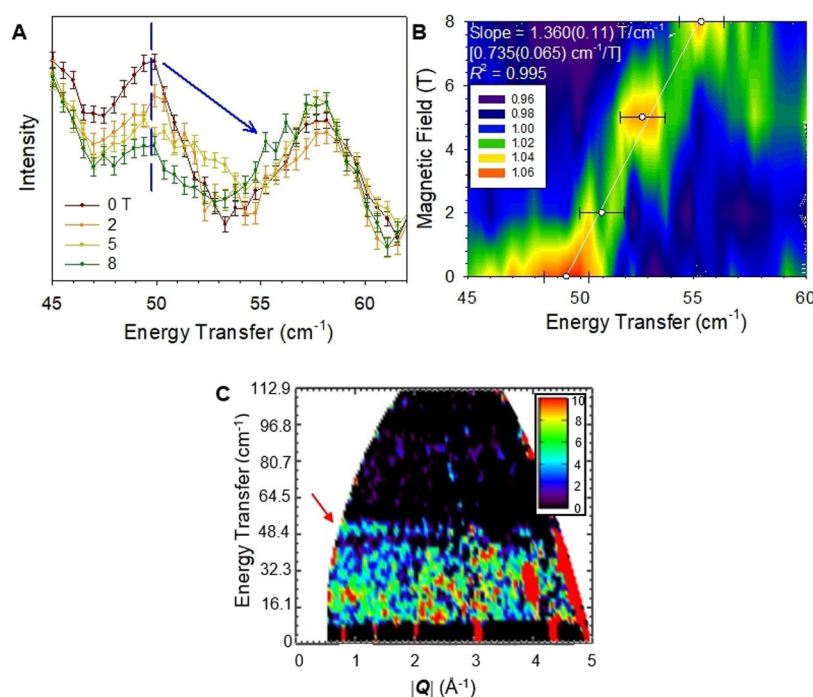


**Figure 2.** (A) INS of **1** at variable magnetic fields showing the ZFS peak at  $49.4(1.0)\text{ cm}^{-1}$ . The  $|Q|$  range is summed at  $1\text{--}3\text{ \AA}^{-1}$ . The dashed, vertical blue line represents the position of the overlapping magnetic and phonon peaks (at 0 T) and the blue arrow represents the blueshift of  $2D'$ . (B) Contour plot of the  $45\text{--}60\text{ cm}^{-1}$  region in the normalized (by average across all fields) INS spectra at different fields showing the ZFS peak at 0 T gradually losing intensity with field increase, as it shifts to approximately  $56\text{ cm}^{-1}$  at 8 T. Overlay is the estimated shift of  $2D'$  based on the intensity changes in the spectra with field. Error is estimated to be  $1.0\text{ cm}^{-1}$ . (C) Change in the peak intensities vs.  $|Q|$  at 2.0 K and zero field. The red arrow indicates the presence of the ZFS peak at low  $|Q|$ , which, as a magnetic peak,<sup>[5b]</sup> gradually loses intensity with increasing  $|Q|$ .

ment and works especially well for protonated samples.<sup>[5b]</sup> However, it does not have the capability to support applied magnetic fields and thus relies only on variable temperatures in the current work. Details of the studies are given in the Supporting Information. In temperature-dependent VISION spectra, one expects the magnetic peak to decrease in intensity at a much faster rate than similar-intensity phonon peaks.<sup>[5]</sup> However, even with the Bose correction applied,<sup>[5a]</sup> no peak in the 40–75  $\text{cm}^{-1}$  region of the variable-temperature INS spectra (Figure S5) stands out with a larger relative intensity change (signifying intensity of magnetic origins). Instead, each peak simultaneously decreases in intensity and shifts with increasing temperature. Despite not revealing the magnetic peak, VISION does give good quality phonon spectra of **1**. Comparing the calculated phonons with INS spectra collected at VISION may reveal the magnetic peak. Phonon spectra obtained from INS experiments and VASP (Vienna ab initio simulation package) calculations as well as the identification of the magnetic peak are discussed below, with resultant spectra compared with experimental spectra in Figure 5 and Figure S9.

As indicated earlier, temperature dependence and diamagnetic controls have been utilized to distinguish magnetic excitations.<sup>[6m,7a]</sup> Such approaches are challenging when the magnetic contribution is weak with strong background.<sup>[8]</sup> The decrease in the intensity of the magnetic peak with increasing  $|Q|$  has been used to identify magnetic peaks.<sup>[6b,20]</sup> This approach also led to the identification of the weak magnetic transition in **1** (Figure 2C). Waldmann and co-workers have used magneto-INS to probe a magnetic transition (at ca. 10  $\text{cm}^{-1}$  at 0 T) in the cluster single-molecule magnet  $[\text{Mn}_{12}\text{O}_{12}(\text{acetate})_{16}(\text{H}_2\text{O})_4]$ .<sup>[9]</sup> We have used INS inside magnetic fields to probe intra-Kramers transitions.<sup>[6b,m]</sup> The current work using CNCS is, to our knowledge, the first conclusive measurements of inter-Kramers doublet (KD) transitions in mononuclear transition-metal complexes by magneto-INS.<sup>[6b,m,9]</sup>

### Far-IR and Raman spectra inside magnetic fields

We have also investigated the magnetic origin of the ZFS peak ( $2D'$ ) in **1** by using far-IR spectroscopy coupled with magnetic fields at 5 K. This method has been utilized to view magnetic transitions on many occasions.<sup>[1d,3a-c,7e]</sup> ZFS transitions between KDs in **1** (e.g.,  $M_S = -3/2 \rightarrow -1/2$  and  $M_S = +3/2 \rightarrow +1/2$ ) are magnetic-dipole allowed by symmetry and selection rules ( $\Delta M_S = 0, \pm 1$ ), as Brackett et al. have shown.<sup>[4]</sup> In  $D_{4d}$  local symmetry around the  $\text{Co}^{\text{II}}$  ion, the magnetic dipole moment operators have  $E_3$  and  $A_2$  symmetries as the rotations ( $R_x, R_y$ ) and  $R_z$ . In the double group  $D_{4d}'$ ,  $M_S = \pm 3/2$  and  $\pm 1/2$  KDs are represented by  $E_{3/2}$  and  $E_{1/2}$ , respectively.<sup>[21]</sup> Thus, both ZFS transitions are far-IR active.<sup>[10,4]</sup>

By using far-IR transmittance of a powder sample (Figure 3 and Figure S6), we can clearly see that a magnetic mode originating at about 50  $\text{cm}^{-1}$  shifts to higher energies with applied field. This mode is exceedingly weak, and cannot be viewed in the raw transmission spectra (Figure 3, middle). Only by normalizing the spectra by the zero-field spectrum ( $T_B/T_0$ , Figure 3, top) or by the average across all fields ( $T_B/T_{\text{AVG}}$ , Figure 3,

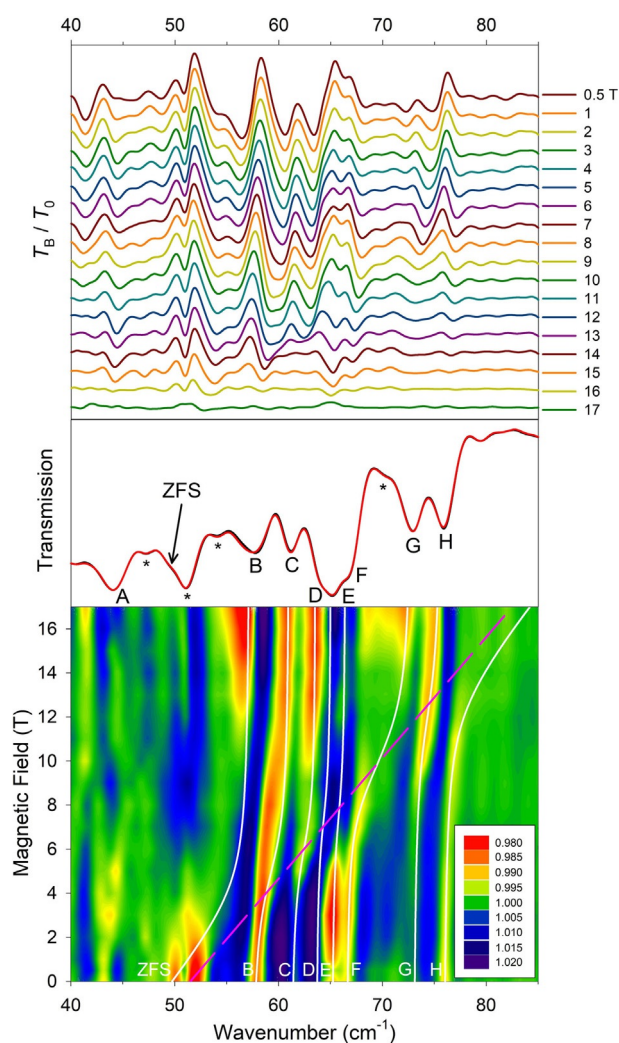


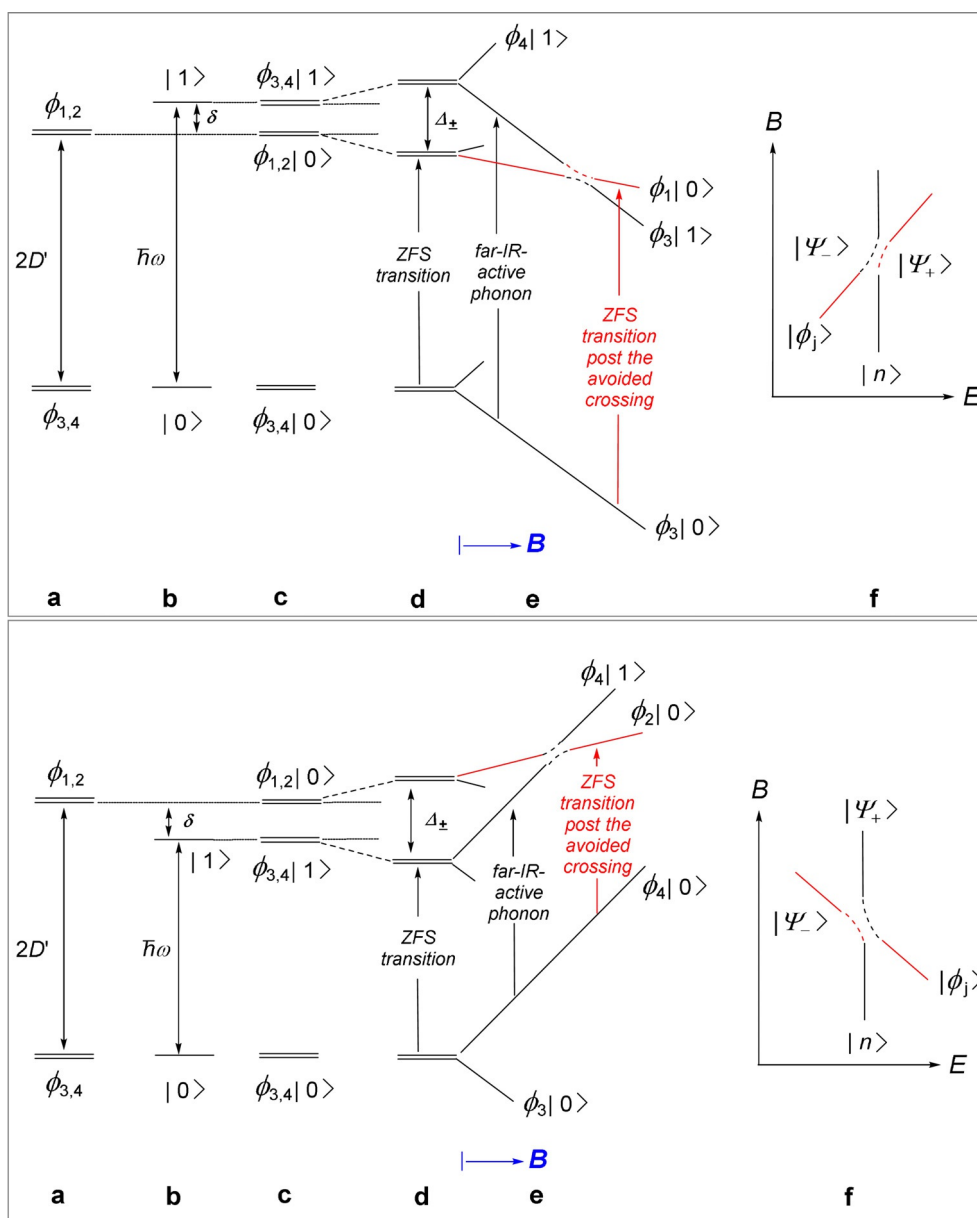
**Figure 3.** Top: Transmission far-IR spectra of **1** using a powder sample and normalized (by 0 T) transmission. Middle: Raw transmission far-IR spectra of **1**. As the changes are small, only the 0 T (black) and 17 T (red) spectra are shown here. The black arrow indicates the origin of the ZFS peak. Peaks labeled by stars are not included in the spin-phonon fit owing to weak intensity. Bottom: Contour plot of normalized (by average) far-IR transmission with fittings displaying the results of the spin-phonon coupling model. All spectra are taken in field increments of 1 T up to 17 T. Letter labels in both plots indicate 0 T positions of far-IR-active phonon peaks. The pink dashed line indicates energies of ZFS transition  $E_{\text{sp}}$  used in the spin-phonon fit. White lines indicate the solution to Equation (3).

bottom) is the shift of this mode revealed. The normalized spectra in Figure 3, top are complicated, indicating the magnetic mode is coupling to several phonon modes. This method does not provide much clarity on the behavior of the ZFS peak. Upon inspection of the contour plot in Figure 3, bottom, there are multiple vertical red-orange lines corresponding to changes in the intensities of multiple phonons (labeled A–H), indicating that each phonon couples with the magnetic peak in some form of spin-phonon coupling. These couplings take the form of avoided crossings, where two transitions repel each other when close in energy. This makes it difficult to locate the exact positions of the magnetic peak. Additionally, the ZFS transition does not appear to have observable intensi-

ty in far-IR, which is not surprising, as magnetic-dipole transitions are typically much weaker in far-IR (or IR) than electric-dipole allowed transitions.<sup>[22]</sup> With field increase, the  $M_S = -3/2 \rightarrow -1/2$  ZFS peak blueshifts to higher energies, eventually residing at its final position at  $55 \text{ cm}^{-1}$  when the ZFS couples to and repels phonon B. This avoided crossing with phonon B is closely followed by several more avoided crossings in quick succession with phonons C–F at 6–9 T. The next avoided crossings occur with phonons G and H at 11–15 T. These are all visible as the bending of the yellow-red lines in Figure 3, bottom. The behavior of the avoided crossings is illustrated in

Scheme 2, with the fit of these avoided crossing described below.

In Scheme 2, the ground spin states  $\varphi_{3,4}|0\rangle$  and the phonon states  $\varphi_{3,4}|1\rangle$  have pairwise identical slopes, whereas  $\varphi_{3,4}|0\rangle$  and the excited ZFS states  $\varphi_{1,2}|0\rangle$  have different slopes. Under applied fields, each set of degenerate states will split into its separate components (e.g.,  $\varphi_{3,4}|0\rangle$  splits into  $\varphi_3|0\rangle$  and  $\varphi_4|0\rangle$ ). The transitions from  $\varphi_3|0\rangle$  to  $\varphi_3|1\rangle$  in Scheme 2, top and  $\varphi_4|0\rangle$  to  $\varphi_4|1\rangle$  in Scheme 2, bottom are in essence field-independent far-IR-active phonon excitations (black arrows). For the blueshifting  $\varphi_3|0\rangle$  ( $M_S = -3/2$ )  $\rightarrow$   $\varphi_1|0\rangle$  ( $M_S = -1/2$ ) transi-



**Scheme 2.** Schematic views of the spin-phonon couplings in 1.  $\varphi_1$ ,  $\varphi_2$ ,  $\varphi_3$ , and  $\varphi_4$  are eigenfunctions of  $M_S = -1/2$ ,  $+1/2$ ,  $-3/2$ , and  $+3/2$  states, respectively.<sup>[23]</sup> Top: Blueshifting  $\varphi_3|0\rangle \rightarrow \varphi_1|0\rangle$  transition. Bottom: Redshifting  $\varphi_4|0\rangle \rightarrow \varphi_2|0\rangle$  transition. (a) Zero-field splitting  $2D'$  of the magnetic/spin quartet ground state. (b) Vibrational states of a selected phonon with eigenfunctions  $|0\rangle$  and  $|1\rangle$  and a small energy separation  $\delta$  above the excited KD  $\varphi_{1,2}$ . (c) Spin-phonon product states with product functions  $\varphi_i|n\rangle$  before vibronic coupling. (d) Vibronic coupling with coupling constant  $A$ , leading to an energy shift and splitting:  $\Delta_{\pm} = (\delta^2 + A^2)^{1/2}$ . (e) Zeeman splitting of vibronic states in a field  $B$  and avoided crossing from the couplings: Top: Between the  $\varphi_1|0\rangle$  and  $\varphi_3|1\rangle$  states; Bottom: Between the  $\varphi_4|1\rangle$  and  $\varphi_2|0\rangle$  states. (f) Avoided crossing in the far-IR spectra based on Equation (3) for blueshifting (top) and redshifting (bottom) transitions.

tion with increasing magnetic fields in Scheme 2, top, the phonon level  $\varphi_3|1\rangle$  approaches the lower magnetic level of the excited KD,  $\varphi_1|0\rangle$ , leading to spin-phonon coupling and a field-dependent transition. For the redshifting  $\varphi_4|0\rangle$  ( $M_S = +3/2$ )  $\rightarrow$   $\varphi_2|0\rangle$  ( $M_S = +1/2$ ) transition with increasing magnetic fields in Scheme 2, bottom, the thermal population of the first excited level,  $\varphi_4|0\rangle$ , at 5 K is small and decreases with larger applied fields. Thus, the transition from this level to the excited KD level  $\varphi_2|0\rangle$  is weak and difficult to observe. With increasing magnetic fields,  $\varphi_4|1\rangle$  approaches  $\varphi_2|0\rangle$ , the upper magnetic level of the excited KD, leading to additional spin-phonon coupling and a field-dependent transition. The ZFS transitions in (d) and (e) of both Scheme 2, top and Scheme 2, bottom are observed in far-IR.

The field-driven avoided crossings in the transmittance far-IR spectra in Figure 3 are characterized in Scheme 2. In the case of two coupled transitions, such as a ZFS peak and a single phonon, we employ a spin-phonon coupling, or avoided-crossing, model to describe their interaction.<sup>[24]</sup> The Hamiltonian for the coupling of magnetic  $|\Psi_{sp}\rangle$  with phonon  $|\Psi_{ph}\rangle$  peaks is given by the following matrix [Equation (3)].<sup>[10]</sup>

$$H = \begin{pmatrix} E_{sp} & \mathcal{A} \\ \mathcal{A} & E_{ph} \end{pmatrix} \quad (3)$$

where  $E_{sp}$  and  $E_{ph}$  are the expected energies of the magnetic (ZFS)  $|\Psi_{sp}\rangle$  and phonon  $|\Psi_{ph}\rangle$  peaks, respectively;  $\mathcal{A}$  is the spin-phonon (or ZFS-phonon) coupling constant between the two peaks. The solution of the matrix gives two energy eigenvalues  $E_{\pm}$  (with the associated avoided-crossing peaks  $|\Psi_{\pm}\rangle$ ), as seen in Scheme 2 f) in the secular Equation (4). The equations give a model to understand the spin-phonon couplings in the far-IR spectra and calculate the coupling constants.

$$\begin{vmatrix} E_{sp} - E_{\pm} & \mathcal{A} \\ \mathcal{A} & E_{ph} - E_{\pm} \end{vmatrix} = 0 \quad (4)$$

This model in Equations (3) and (4) can be expanded to an  $8 \times 8$  matrix in Equation (5) to account for all coupled phonons in Figure 3 simultaneously. The ZFS peak ( $E_{sp}$ ) was modeled every 0.5 T from  $51.5 \text{ cm}^{-1}$  at 0 T to  $82.5 \text{ cm}^{-1}$  at 17 T for the transmittance peak (pink dashed line in Figure 3). If the spectra are instead fit by using multiple  $2 \times 2$  matrices, the coupling constants are not appreciably different.

$$H = \begin{pmatrix} E_{sp} & \mathcal{A}_1 & \mathcal{A}_2 & \mathcal{A}_3 & \mathcal{A}_4 & \mathcal{A}_5 & \mathcal{A}_6 & \mathcal{A}_7 \\ \mathcal{A}_1 & E_{ph1} & 0 & 0 & 0 & 0 & 0 & 0 \\ \mathcal{A}_2 & 0 & E_{ph2} & 0 & 0 & 0 & 0 & 0 \\ \mathcal{A}_3 & 0 & 0 & E_{ph3} & 0 & 0 & 0 & 0 \\ \mathcal{A}_4 & 0 & 0 & 0 & E_{ph4} & 0 & 0 & 0 \\ \mathcal{A}_5 & 0 & 0 & 0 & 0 & E_{ph5} & 0 & 0 \\ \mathcal{A}_6 & 0 & 0 & 0 & 0 & 0 & E_{ph6} & 0 \\ \mathcal{A}_7 & 0 & 0 & 0 & 0 & 0 & 0 & E_{ph7} \end{pmatrix} \quad (5)$$

This matrix includes seven phonons ( $E_{ph*i*}, i=1-7$ ) and their respective coupling constants ( $\mathcal{A}_i, i=1-7$ ), assuming that the magnetic peak does not couple to one phonon at a time, but instead couples to all phonons simultaneously. The coupling constants from the fit by Equation (5) for the transmittance spectra in Figure 3 are given in Table 1. This is an empirical fit, and the coupling between the magnetic peak and a single phonon is present across the entire energy range. The coupling strengthens as the spin and phonon modes approach each other. Thus, we fit all modes simultaneously.

**Table 1.** Peak positions and coupling constants for spin-phonon fit parameters of both transmittance and reflectance peaks in Figure 3 and Figure S7. The phonon that overlaps the ZFS peak was not included in the fit owing to its close proximity and lack of visible coupling.

Phonon	A	B	C	D	E	F	G	H
Transmittance peak [ $\text{cm}^{-1}$ ]	N/A	57.3(5)	61.1(5)	63.6(5)	65.1(7)	66.5(5)	72.9(5)	75.8(4)
$\mathcal{A}$ [ $\text{cm}^{-1}$ ]	N/A	2.2(6)	1.9(4)	1.3(5)	1.4(6)	1.5(4)	2.0(5)	2.3(6)
Reflectance peak [ $\text{cm}^{-1}$ ]	44.6(4)	58.3(3)	62.4(4)	64.8(9)	66.0(4)	68.0(4)	73.6(5)	76.2(5)
$\mathcal{A}$ [ $\text{cm}^{-1}$ ]	0.7(3)	1.7(4)	1.5(5)	1.0(5)	1.0(5)	1.4(6)	1.4(7)	1.4(4)

The fit relies on a visual agreement between the white lines and the red/orange/yellow normalized intensities in the contour plot of Figure 3, bottom. On close examination of the contour plot, it is clear that the white lines do not line up with phonons B and C very well between 4 and 12 T, even though each subsequent peak lines up well. Figure S6 shows that it is possible to fit these peaks well if we assume the presence of a second, slower blueshifting magnetic peak that begins at the same position ( $E_{sp} = 51.5 \text{ cm}^{-1}$ ) and shifts to about  $71 \text{ cm}^{-1}$  by 17 T. This second shift is similar to that of the reflectance shift by the field in Figure S7, as explained below. This indicates that, as expected, some powders of **1** in the transmittance spectra in Figure 3 are in a similar orientation as the single crystal used in the reflectance spectra (Figure S7). For the powder sample for Figure 3, we expect to see an average of three orientations ( $x, y,$  and  $z$ ). Owing to the near lack of anisotropy in the  $xy$  plane of the molecule ( $E \approx 0$ ), it is likely that there are two shifting peaks corresponding to the  $xy$  and  $z$  directions, respectively.

Reflectance FIRMS spectra (Figure S7) using a single crystal of **1** oriented in the Voigt geometry<sup>[25]</sup> relative to the magnetic field show similar results, including the spin-phonon couplings of the blueshifting transition as avoided crossings. A photo of the crystal on the sample holder is given in Figure S7, top. It should be noted that the crystal oriented in the Voigt geometry<sup>[25]</sup> here is likely different from the orientations of the two large crystals (relative to the external magnetic field) used in INS studies, as photos in Figure S7, top for the former and Figures S1, S2 for the latter show. Additionally, the reflectance spectra reveal the presence of a weak redshifting peak observable up to 8 T, where it has an avoided crossing with phonon

A at  $44\text{ cm}^{-1}$ . We attribute this peak to the  $M_S = +3/2 \rightarrow +1/2$  transition (Figure 1, right), which is expected to redshift with field. Owing to the increasing energy of the  $M_S = +3/2$  state with applied field, it is expected that any transition stemming from this state gradually disappears with increasing field owing to the decreasing Boltzmann distribution at the  $M_S = +3/2$  state. The coupling of the redshifted ZFS peak ( $E_{sp}$ ) with phonon A at  $44.6(4)\text{ cm}^{-1}$  was modeled every  $0.5\text{ T}$  from  $49.0\text{ cm}^{-1}$  at  $0\text{ T}$  to  $38.0\text{ cm}^{-1}$  at  $17\text{ T}$  by the  $2 \times 2$  matrix in Equation (3), yielding the coupling constant  $\Delta = 0.7(3)\text{ cm}^{-1}$  (pink dashed line on the left in Figure S7). In addition, the coupling of the blueshifted ZFS peak ( $E_{sp}$ ) with phonons B–H was modeled every  $0.5\text{ T}$  from  $50.5\text{ cm}^{-1}$  at  $0\text{ T}$  to  $74.0\text{ cm}^{-1}$  at  $17\text{ T}$  by the  $8 \times 8$  matrix in Equation (5), yielding the coupling constants in Table 1 (pink dashed line on the right in Figure S7). The couplings from the reflectance far-IR spectra of **1** (Figure S7) are consistent with those from the transmittance spectra of the powder sample in Figure 3. However, the peak positions and coupling constants change slightly, as shown in Table 1.

It is possible that there are other couplings that are too weak to be observed in the normalized spectra. The ZFS peak lies close to and is likely coupled with a phonon at  $51\text{ cm}^{-1}$  at zero field. As shown in Figure 3, top, there are three peaks labeled with an asterisk (\*), including the aforementioned  $51.0\text{ cm}^{-1}$  peak. These phonons were not considered in the fit for either far-IR spectra as avoided crossings with them were not observed. It is likely that they couple with the ZFS peak, but their intensity is too weak to be noticeable, even in the contour plot. Each of these peaks could potentially be inserted into the fit by expanding the matrix in Equation (5) to an  $11 \times 11$  matrix. The results of this expanded fit are shown in Figure S8 for completeness.

Using the positions at  $0$  and  $17\text{ T}$  in Figure 3, bottom (pink dashed line) gives an estimated slope of  $1.82(5)\text{ cm}^{-1}\text{ T}^{-1}$  for the fast-shifting peak in the powder sample. Additionally, the slope of the second, slower transmittance peak is about  $1.15(5)\text{ cm}^{-1}\text{ T}^{-1}$  (Figure S6, pink dashed line). From a visual perspective, the shift in the FIRMS reflectance spectra (Figure S7) starts out almost identical to that of the slower moving transmittance peak, and then increases to a rate similar to that of the faster one. However, when fitted using Equation (5), the shift rate is determined to be about  $1.38(10)\text{ cm}^{-1}\text{ T}^{-1}$ . This fits reasonably well for most of the recorded spectra. However, it deviates slightly around  $16\text{--}17\text{ T}$ , as the intensity does not line up perfectly with the fit, which could indicate that the shift rate increases slightly. In comparison, the slope is  $0.85(8)\text{ cm}^{-1}\text{ T}^{-1}$  from the INS spectra by using crystals oriented along the  $z$  axis (Figure 4). It should be noted that the slope relies on the crystal orientation. Both the INS and far-IR reflectance spectra are measurements using single crystals at likely different crystal orientations (Figures S1, S2, and S7, top for INS and far-IR reflectance), whereas the far-IR transmittance is a powder measurement. The slopes of each method are compared in Figure 4.

Raman spectra of **1** in  $0\text{--}14\text{ T}$  magnetic fields are given in Figure S9. No observable magnetic feature or spin-phonon

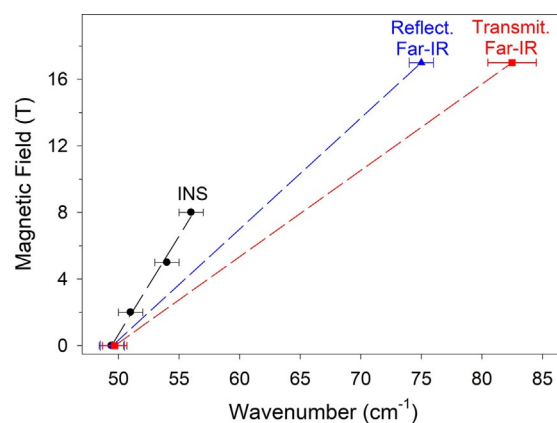


**Figure 4.** Comparison of FIRMS transmission (red), FIRMS reflectance (blue), and INS (black) magnetic peak positions with field. Note that the far-IR points do not strictly correspond to the magnetic transition  $M_S = -3/2 \rightarrow -1/2$ , as there are numerous avoided crossings in the region. Instead, they are simply indications of the direction and rate of the magnetic transition shifts. The errors were estimated to be  $1\text{ cm}^{-1}$ . The errors grow larger in the far-IR spectra with increasing fields, reaching approximately  $2\text{ cm}^{-1}$  for the points at  $17\text{ T}$ . The different slopes from the INS and FIRMS reflectance spectra are the result of likely different crystal orientations as shown in Figures S1, S2, and S7, top.

coupling with the Raman-active phonons was found between  $50$  and  $70\text{ cm}^{-1}$  with or without an applied field. If the magnetic ZFS transition in **1** is present in Raman, it is vanishingly weak and not clearly observed. It is currently not clear why apparently no such coupling with the Raman-active phonon occurs in **1**.

#### Calculation of phonons in the crystal of **1**

Accurate phonon calculations, such as those by the method used here, are needed as a first step to understand the atomic displacements in SMMs that lead to spin-phonon coupling. The VASP phonon calculation of the INS spectrum was completed by using the structure from single-crystal neutron diffraction at  $100\text{ K}$  at TOPAZ. Only the database of irreducible representations for a few point group types at the  $\Gamma$  point are implemented in Phonopy.<sup>[26]</sup> The point group for **1**,  $2/m$  (space group 15,  $C_{2h}$ ), was used to assign symmetries to each phonon (Table S2). It is important to note that these assignments come from the point group of the unit cell ( $C_{2h}$ ) and not the local symmetry of the  $\text{Co}(\text{12C4})_2^{2+}$  ion ( $D_4$  or  $\sim D_{4d}$ ). Figure 5 compares the Raman as well as experimental and calculated far-IR and INS spectra (by VISION) at  $5\text{ K}$  for the  $20\text{--}1000\text{ cm}^{-1}$  region. The  $1000\text{--}4000\text{ cm}^{-1}$  range of the experimental INS spectrum at  $5\text{ K}$  and calculated INS phonons are given in Figure S10. Calculated INS mode intensities are given in Figure S11 and Table S2. Movies (animations) of 19 phonons at  $42.44\text{--}57.64\text{ cm}^{-1}$  near the magnetic peak are provided in the Supporting Information.

Overall, there is a good match between experimental and calculated INS and far-IR spectra in Figure 5 and Figure S9 above  $150\text{ cm}^{-1}$ . However, low-energy modes are difficult to calculate accurately. Additionally, the calculated peaks shown

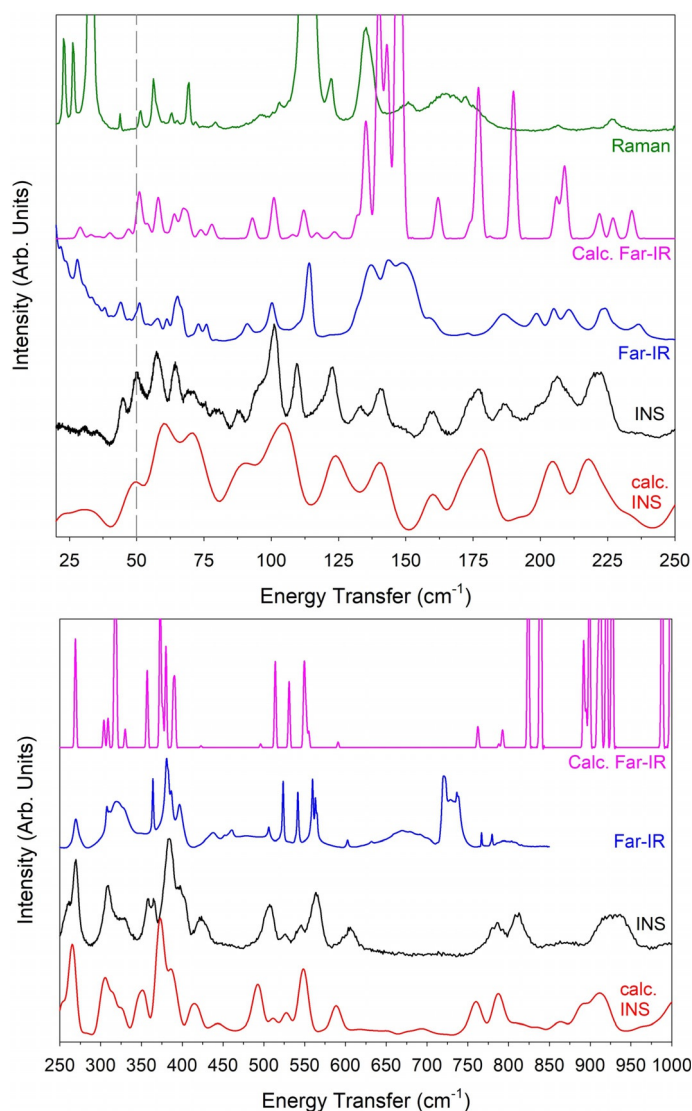


**Figure 5.** Top: The 25–250  $\text{cm}^{-1}$  region of experimental Raman, far-IR, and INS at 0 T and calculated far-IR and INS spectra. The vertical dashed line indicates the position of the ZFS peak. Bottom: The 250–1000  $\text{cm}^{-1}$  range of calculated and experimental far-IR and INS spectra (VISION) at 5 K. The experimental far-IR data approached zero transmittance around 800  $\text{cm}^{-1}$  owing to the settings of the spectrometer. Far-IR data here are baseline-corrected for easy comparison.

in Figure 5 do not include only one calculated mode. Instead, each peak consists of one or more modes of similar vibrational motion (Table S2). As INS has no vibrational selection rules,<sup>[27]</sup> all phonon modes in a molecule are expected to be observed in INS. In comparison, as optical spectroscopies, far-IR and Raman each have symmetry-based vibrational selection rules. Thus, there are certain forbidden modes in each spectroscopy. In addition, INS generally reflects the dynamics of the nuclei in the vibrations, giving a description of nuclear dynamics in a molecule. Far-IR and Raman, in contrast, show the changes in electric dipole and polarizability of the electrons in a molecule, respectively, as a result of the vibrations. It should be pointed out that the current calculations do not account for any modes of magnetic origin or spin-phonon coupling.

## Remarks on magnetic relaxation of 1

In our previous studies on alternating current (AC) magnetic susceptibility,<sup>[2]</sup> we analyzed the Arrhenius plot of  $\ln \tau$  as a function of  $T^{-1}$  (Figure 6) at high temperatures. The plot was

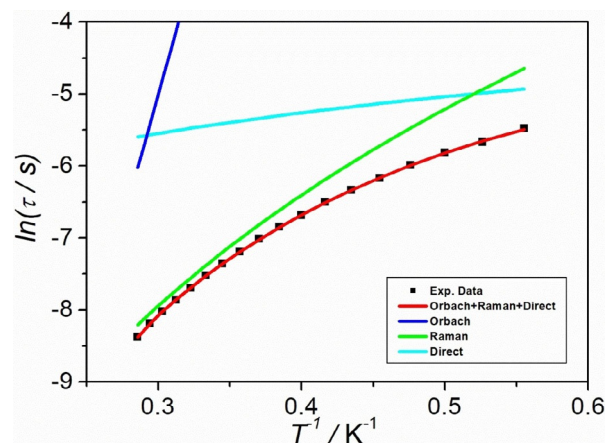


**Figure 6.** Relaxation time of the magnetization  $\ln \tau$  vs.  $T^{-1}$  plot for 1. The red line represents the fit to the direct, Raman, and Orbach processes simultaneously. The light blue, green, and blue curves represent the contributions of the direct, Raman, and Orbach processes, respectively.

constructed from the peaks of out-of-phase susceptibility component  $\chi''$  from the frequency-dependent AC data, by a fit to the Arrhenius law  $\tau = \tau_0 \exp(U_{\text{eff}}/kT)$ , affording an effective energy barrier to spin-reversal  $U_{\text{eff}} = 17.0 \text{ cm}^{-1}$  and a pre-exponential factor of  $\tau_0 = 1.5 \times 10^{-6} \text{ s}$ . Such a linear treatment of the experimental data at the high-temperature range has been extensively used in the estimation of the energy barrier for the thermally activated Orbach process especially for the SMMs based on polynuclear metal complexes.<sup>[11]</sup> It should be emphasized that this approach was based on the assumption that the Orbach relaxation process is the dominant mechanism in the high-temperature range. Recent studies on single-ion magnets (SIMs), those SMMs containing one magnetic center, have shown the shortcomings of such an estimation because other relaxation processes, such as the Raman-like and direct processes, are also operative in the studied temperature ranges.<sup>[3c,g,7g,28]</sup> Analyses of d-<sup>[3c,g,28a-c]</sup> and f-SIMs<sup>[7g,28d,e]</sup> by using the multi-process model have been reported. In fact, the Orbach mechanism is not necessarily the dominant process.<sup>[3c,g,7g,28]</sup> In some cases, the Raman process was found to be the only relaxation mechanism at least in the investigated temperature range.<sup>[6i,29]</sup> Thus, a detailed analysis considering all the possible relaxation processes is required to probe the relaxation processes of SMMs.<sup>[3c,g,7g,28]</sup> According to the definition of the Orbach mechanism,<sup>[30]</sup> the energy barrier  $U_{\text{eff}} = 17.0 \text{ cm}^{-1}$  implies a gap of  $17.0 \text{ cm}^{-1}$  between the ground KD ( $M_S = \pm 3/2$ ) and the excited KD ( $M_S = \pm 1/2$ ) in 1. In light of the ZFS parameter  $2D'$  [ $49.4(1.0) \text{ cm}^{-1}$ ] determined by INS and far-IR in the present study, clearly the energy barrier of  $17.0 \text{ cm}^{-1}$  was underestimated. The curvature in the Arrhenius plot (Figure 6) implies a non-negligible contribution of the

direct and/or Raman processes in determining the relaxation rate. Therefore, the relaxation times at different temperatures were fitted again with Equation (6) considering the direct, Raman, and Orbach processes together.<sup>[30]</sup>

$$\tau^{-1} = AT + CT^n + \tau_0^{-1} \exp(-U_{\text{eff}}/kT) \quad (6)$$

where the first, second, and third terms represent the contributions of the direct, Raman, and Orbach processes, respectively. For the Raman process,  $n=9$  is expected in Kramers ions whereas  $n=1-6$  is reasonable when both optical and acoustic phonons are involved.<sup>[30]</sup> The fitting parameters are  $A=77.03 \text{ s}^{-1} \text{ K}^{-1}$ ,  $C=4.49 \text{ s}^{-1} \text{ K}^{-n}$ ,  $n=5.35$ ,  $\tau_0=3.75 \times 10^{-12} \text{ s}^{-1}$  with  $U_{\text{eff}}$  fixed at  $49.4 \text{ cm}^{-1}$ . The fitting curves are depicted in Figure 6, from which the contributions of the direct, Raman, and Orbach processes are also shown. It is clear that the Raman process is the major mechanism and that the direct and Orbach processes only make small contributions above 2 K.

The above work stimulated our attempt to fit the relaxation times by using the Raman-like process as the only mechanism with a power law  $\tau^{-1}=CT^n$ , assuming that the contribution of the Orbach or direct mechanism can be neglected. A reasonable agreement is found with the parameters  $C=16.04 \text{ s}^{-1} \text{ K}^{-n}$  and  $n=4.35$  (Figure S12), suggesting that our previous estimation of the energy barrier for the spin-reversal is incorrect and that the Raman-like process dominates in the studied temperature range. The  $n$  value of 4.35 indicates that the optical acoustic Raman-like mechanism occurs in the magnetic relaxation of **1**.<sup>[31]</sup>

## Conclusion

The work with the single crystals and powders of  $[\text{Co}(\text{12C4})_2(\text{I}_3)_2(\text{12C4})]$  (**1**) reveals the power of spectroscopic techniques to directly probe the magnetic excited level at  $2D'$  and spin-phonon couplings. Far-IR studies of **1** have not only confirmed the ZFS position observed in INS, but also have shown that the weak ZFS peak couples with multiple far-IR active phonons simultaneously. It is likely that if higher fields were used, the magnetic peak would continue to shift and experience additional avoided crossings with higher energy phonons.

The INS work demonstrates that deuterated samples are not required to study magnetic excitations by INS, even in the region around  $50 \text{ cm}^{-1}$  where phonons are prevalent. Two unique features of the current work are the use of oriented single crystals of a metal complex and a magnet in INS. Their combined use at CNCS is crucial here, when the variable-temperature INS alone failed to directly determine the ZFS peak. The use of single crystals in INS provided a clear transfer of the magnetic intensity in the spectra without the broadening typically observed for powder samples. Many low-energy phonons near the magnetic peak in **1** are revealed in the INS spectra, which the spin can interact with. The INS spectrum of **1** at VISION made it possible to compare observed phonons with the calculated ones.

## Experimental Section

The INS experiments with the single crystals were conducted at CNCS.<sup>[18a]</sup> The crystals were glued to the sample plate with fluoro-polymer glue CYTOP (with no H atoms). The 8 T magnet, which blocks approximately 70% of detectors, was placed in the sample environment. Each field measurement (0, 2, 5, and 8 T) was run for about 8 h. The incident energy and temperature for the measurements were  $12.07 \text{ meV}$  ( $97.34 \text{ cm}^{-1}$ ) and 2.0 K, respectively.

For variable-temperature INS at VISION, the sample (2 g) was sealed in an aluminium container. INS spectra of **1** were measured at 10, 25, 50, 100, and 125 K. The design at VISION offers two banks of detectors for both forward (low  $|Q|$ ) and back (high  $|Q|$ ) scattering of neutrons.<sup>[19a]</sup> The phonon population effect was corrected by normalizing the INS intensity at energy transfer  $\omega$  with  $\coth(\hbar\omega/2kT)$ .<sup>[5a]</sup>

Far-IR and Raman spectroscopic studies were conducted at the National High Magnetic Field Laboratory (NHMFL) at Florida State University. For far-IR spectra, the powdered samples were placed in a sample holder and mixed with eicosane to hold them in place. Spectra were collected at 5 K by using a Bruker Vertex 80v FTIR spectrometer coupled with a superconducting magnet (SCM) with fields up to 17 T. Reflectance spectra were collected by using the same spectrometer and magnet, with a single crystal oriented in the Voigt geometry relative to the magnetic field, as shown in Figure S7, top. Far-IR transmittance reaches zero at about  $800 \text{ cm}^{-1}$  owing to the experimental setting of the FTIR spectrometer.

For calculations on **1** by VASP, geometry optimizations were performed on the single-crystal neutron structure of **1** at 100 K. The optimized structure completed at 0 T was used for the phonon calculations. Spin-polarized, periodic DFT calculations were performed by using VASP with the Projector Augmented Wave (PAW) method and the local density approximation (GGA) +  $U$  ( $U=5.37$ ) exchange correlation functional. An energy cut off was 900 eV for the plane-wave basis of the valence electrons. Total energy tolerance for electronic structure minimization was  $10^{-8}$  eV. The optB86b-vdW, a non-local correlation functional that roughly accounts for dispersion interactions, was applied. For the structure relaxation, a  $1 \times 1 \times 1$  Monkhorst-Pack mesh was applied. The INS spectrum and peak intensities for both forward and backscattering were calculated by using OCLIMAX, a versatile INS simulation program developed at ORNL.<sup>[32]</sup> Phonopy, an open source phonon analyzer, was used to create a  $1 \times 1 \times 1$  supercell structure and extract phonon symmetries. VASP was then employed to calculate the force constants on the supercell in real space by using DFT. The IR intensities and spectrum were calculated directly from the VASP output using a constant resolution of  $1 \text{ cm}^{-1}$ .

Additional experimental details are given in the Supporting Information.

## Acknowledgments

The authors thank financial support by the US National Science Foundation (CHE-1633870 and CHE-1900296 to Z.-L.X.), Department of Navy HBCU/MI program (K.T.), and a Shull Wollan Center Graduate Research Fellowship (S.E.S.). Acknowledgment is also made to the Donors of the American Chemical Society Petroleum Research Fund for partial support of this work and to Jonathan Ludwig for help. This research used resources at the Spallation Neutron Source, a Department of Energy (DOE) Office of Science User Facility operated by ORNL. Computations

al resources for the VASP DFT calculations were made available through the VirtuES and ICE-MAN projects, funded by the Laboratory Directed Research and Development at ORNL. A portion of this work was performed at the National High Magnetic Field Laboratory, which is supported by NSF Cooperative Agreement No. DMR-1644779 and the State of Florida. NSF's ChemMatCARS Sector 15 is principally supported by the Divisions of Chemistry (CHE) and Materials Research (DMR), NSF, under grant number NSF/CHE-1834750. Use of the Advanced Photon Source, an Office of Science User Facility operated for the DOE Office of Science by Argonne National Laboratory, was supported by the DOE under Contract No. DE-AC02-06CH11357.

## Conflict of interest

The authors declare no conflict of interest.

**Keywords:** cobalt · magnetic transitions · single-molecule magnets (SMMs) · spin-phonon coupling · vibrational spectroscopies

- [1] a) C. Benelli, D. Gatteschi, *Introduction to Molecular Magnetism, Ch. 13, Single Ion Magnet (SIM)*, Wiley-VCH, Weinheim, **2015**, pp. 217–237; b) J. M. Frost, K. L. M. Harriman, M. Murugesu, *Chem. Sci.* **2016**, *7*, 2470–2491; c) R. A. Layfield, *Organometallics* **2014**, *33*, 1084–1099; d) J. Krzystek, J. Telsler, *Dalton Trans.* **2016**, *45*, 16751–16763; e) E. J. L. McInnes, R. E. P. Winpenny in *Comprehensive Inorganic Chemistry II* (Ed.: K. Poepelmeier), Elsevier, Amsterdam, **2013**, pp. 371–395; f) F. Neese, D. A. Pantazis, *Faraday Discuss.* **2011**, *148*, 229–238; g) *Molecular Nanomagnets and Related Phenomena* (Ed.: S. Gao), Springer, Berlin, **2015**; h) P. Zhang, L. Zhang, J. Tang, *Dalton Trans.* **2015**, *44*, 3923–3929; i) J.-L. Liu, Y.-C. Chen, M.-L. Tong, *Chem. Soc. Rev.* **2018**, *47*, 2431–2453; j) G. A. Craig, M. Murrie, *Chem. Soc. Rev.* **2015**, *44*, 2135–2147; k) J. D. Rinehart, J. R. Long, *Chem. Sci.* **2011**, *2*, 2078–2085; l) D. Gatteschi, R. Sessoli, *Angew. Chem. Int. Ed.* **2003**, *42*, 268–297; *Angew. Chem.* **2003**, *115*, 278–309; m) S. Demir, I.-R. Jeon, J. R. Long, T. D. Harris, *Coord. Chem. Rev.* **2015**, *289*, 149–176; n) M. Dey, N. Gogoi, *Angew. Chem. Int. Ed.* **2013**, *52*, 12780–12782; *Angew. Chem.* **2013**, *125*, 13014–13016; o) R. Boča, *Coord. Chem. Rev.* **2004**, *248*, 757–815; p) M. Shatruk, S. Gómez-Coca, K. R. Dunbar in *Molecular Magnetic Materials: Concepts and Applications* (Eds.: B. Sieklucka, D. Pinkowicz), Wiley-VCH, Weinheim, **2017**, pp. 29–77; q) M. Yamashita, K. Katoh in *Molecular Magnetic Materials: Concepts and Applications* (Eds.: B. Sieklucka, D. Pinkowicz), Wiley-VCH, Weinheim, **2017**, pp. 79–101; r) D. Gatteschi, R. Sessoli, J. Villain, *Molecular Nanomagnets*, Oxford University Press, Oxford, **2006**; s) S. E. Stavretis, E. Mamontov, D. H. Moseley, Y. Cheng, L. L. Daemen, A. J. Ramirez-Cuesta, Z.-L. Xue, *Phys. Chem. Chem. Phys.* **2018**, *20*, 21119–21126.
- [2] a) L. Chen, J. Wang, J.-M. Wei, W. Wernsdorfer, X.-T. Chen, Y.-Q. Zhang, Y. Song, Z.-L. Xue, *J. Am. Chem. Soc.* **2014**, *136*, 12213–12216; b) J.-M. Wei, Y.-Q. Zhang, *Inorg. Chem.* **2015**, *54*, 1203–1205.
- [3] a) K. Ray, A. Begum, T. Weyhermüller, S. Piligkos, J. van Slageren, F. Neese, K. Wieghardt, *J. Am. Chem. Soc.* **2005**, *127*, 4403–4415; b) Y. Rechkemmer, J. E. Fischer, R. Marx, M. Dörfel, P. Neugebauer, S. Horvath, M. Gysler, T. Brock-Nannestad, W. Frey, M. F. Reid, J. van Slageren, *J. Am. Chem. Soc.* **2015**, *137*, 13114–13120; c) Y. Rechkemmer, F. D. Breitgoff, M. van der Meer, M. Atanasov, M. Haki, M. Orlita, P. Neugebauer, F. Neese, B. Sarkar, J. van Slageren, *Nat. Commun.* **2016**, *7*, 10467; d) P. C. Bunting, M. Atanasov, E. Damgaard-Møller, M. Perfetti, I. Crassee, M. Orlita, J. Overgaard, J. van Slageren, F. Neese, J. R. Long, *Science* **2018**, *362*, eaat7319; e) S.-D. Jiang, D. Maganas, N. Levesanos, E. Ferentinos, S. Haas, K. Thirunavukkuarasu, J. Krzystek, M. Dressel, L. Bogani, F. Neese, P. Kyritsis, *J. Am. Chem. Soc.* **2015**, *137*, 12923–12928; f) A. Świtlicka, B. Machura, M. Penkala, A. Bieńko, D. C. Bieńko, J. Titiš, C. Rajnák, R. Boča, A. Ozarowski, M. Ozerov, *Inorg. Chem.* **2018**, *57*, 12740–12755; g) M. A. Hay, A. Sarkar, G. A. Craig, L. Bhaskaran, J. Nehrkorn, M. Ozerov, K. E. R. Marriott, C. Wilson, G. Rajaraman, S. Hill, M. Murrie, *Chem. Sci.* **2019**, *10*, 6354–6361.
- [4] a) G. C. Brackett, Ph.D. dissertation, University of California, Berkeley, **1970**; b) G. C. Brackett, P. L. Richards, W. S. Caughey, *J. Chem. Phys.* **1971**, *54*, 4383–4401.
- [5] a) P. C. H. Mitchell, S. F. Parker, A. J. Ramirez-Cuesta, J. Tomkinson, *Vibrational Spectroscopy with Neutrons: With Applications in Chemistry, Biology, Materials Science and Catalysis*, World Scientific, Singapore, **2005**, pp. 552–558; b) Z.-L. Xue, A. J. Ramirez-Cuesta, C. M. Brown, S. Calder, H. Cao, B. C. Chakoumakos, L. L. Daemen, A. Huq, A. I. Kolesnikov, E. Mamontov, A. A. Podlesnyak, X. Wang, *Eur. J. Inorg. Chem.* **2019**, 1065–1089.
- [6] a) D. Pinkowicz, H. I. Southerland, C. Avendaño, A. Prosvirin, C. Sanders, W. Wernsdorfer, K. S. Pedersen, J. Dreiser, R. Clérac, J. Nehrkorn, G. G. Simoneoni, A. Schnegg, K. Holldack, K. R. Dunbar, *J. Am. Chem. Soc.* **2015**, *137*, 14406–14422; b) L. Chen, H.-H. Cui, S. E. Stavretis, S. C. Hunter, Y.-Q. Zhang, X.-T. Chen, Y.-C. Sun, Z. Wang, Y. Song, A. A. Podlesnyak, Z.-W. Ouyang, Z.-L. Xue, *Inorg. Chem.* **2016**, *55*, 12603–12617; c) J. Dreiser, A. Schnegg, K. Holldack, K. S. Pedersen, M. Schau-Magnussen, J. Nehrkorn, P. Tregenna-Piggott, H. Mutka, H. Weihe, J. Bendix, O. Waldmann, *Chem. Eur. J.* **2011**, *17*, 7492–7498; d) H. Andres, R. Basler, H.-U. Güdel, G. Aromí, G. Christou, H. Büttner, B. Rufflé, *J. Am. Chem. Soc.* **2000**, *122*, 12469–12477; e) R. Basler, A. Sieber, G. Chaboussant, H. U. Güdel, N. E. Chakov, M. Soler, G. Christou, A. Desmedt, R. Lechner, *Inorg. Chem.* **2005**, *44*, 649–653; f) Y. Zhong, M. P. Sarachik, J. R. Friedman, R. A. Robinson, T. M. Kelley, H. Nakotte, A. C. Christianson, F. Trouw, S. M. J. Aubin, D. N. Hendrickson, *J. Appl. Phys.* **1999**, *85*, 5636–5638; g) I. Mirebeau, M. Hennion, H. Casalta, H. Andres, H. U. Güdel, A. V. Irodova, A. Caneschi, *Phys. Rev. Lett.* **1999**, *83*, 628–631; h) R. Basler, P. L. W. Tregenna-Piggott, H. Andres, C. Dobe, H.-U. Güdel, S. Janssen, G. J. McIntyre, *J. Am. Chem. Soc.* **2001**, *123*, 3377–3378; i) E. Colacio, J. Ruiz, E. Ruiz, E. Cremades, J. Krzystek, S. Carretta, J. Cano, T. Guidi, W. Wernsdorfer, E. K. Brechin, *Angew. Chem. Int. Ed.* **2013**, *52*, 9130–9134; *Angew. Chem.* **2013**, *125*, 9300–9304; j) A. Sieber, C. Boskovic, R. Bircher, O. Waldmann, S. T. Ochsenein, G. Chaboussant, H. U. Güdel, N. Kirchner, J. van Slageren, W. Wernsdorfer, A. Neels, H. Stoeckli-Evans, S. Janssen, F. Juranyi, H. Mutka, *Inorg. Chem.* **2005**, *44*, 4315–4325; k) M. Sigrist, P. L. W. Tregenna-Piggott, K. S. Pedersen, M. A. Sørensen, A.-L. Barra, J. Hauser, S.-X. Liu, S. Decurtins, H. Mutka, J. Bendix, *Eur. J. Inorg. Chem.* **2015**, 2683–2689; l) R. Bircher, G. Chaboussant, S. T. Ochsenein, F. Fernandez-Alonso, H. U. Güdel, E. K. Brechin, *Polyhedron* **2005**, *24*, 2455–2458; m) S. E. Stavretis, Y. Cheng, L. L. Daemen, C. M. Brown, D. H. Moseley, E. Bill, M. Atanasov, A. J. Ramirez-Cuesta, F. Neese, Z.-L. Xue, *Eur. J. Inorg. Chem.* **2019**, 1119–1127.
- [7] a) M. J. Giansiracusa, M. Vongi, W. Van den Heuvel, R. W. Gable, B. Moubarak, K. S. Murray, D. Yu, R. A. Mole, A. Soncini, C. Boskovic, *Inorg. Chem.* **2016**, *55*, 5201–5214; b) M. Kofu, O. Yamamuro, T. Kajiwara, Y. Yoshimura, M. Nakano, K. Nakajima, S. Ohira-Kawamura, T. Kikuchi, Y. Inamura, *Phys. Rev. B* **2013**, *88*, 064405; c) M. Vongi, M. J. Giansiracusa, W. Van den Heuvel, R. W. Gable, B. Moubarak, K. S. Murray, D. Yu, R. A. Mole, A. Soncini, C. Boskovic, *Inorg. Chem.* **2017**, *56*, 378–394; d) K. Prša, J. Nehrkorn, J. Corbey, W. Evans, S. Demir, J. Long, T. Guidi, O. Waldmann, *Magnetochemistry* **2016**, *2*, 45; e) R. Marx, F. Moro, M. Dorfel, L. Ungur, M. Waters, S. D. Jiang, M. Orlita, J. Taylor, W. Frey, L. F. Chibotaru, J. van Slageren, *Chem. Sci.* **2014**, *5*, 3287–3293; f) M. L. Baker, T. Tanaka, R. Murakami, S. Ohira-Kawamura, K. Nakajima, T. Ishida, H. Nojiri, *Inorg. Chem.* **2015**, *54*, 5732–5738; g) K. S. Pedersen, L. Ungur, M. Sigrist, A. Sundt, M. Schau-Magnussen, V. Vieru, H. Mutka, S. Rols, H. Weihe, O. Waldmann, L. F. Chibotaru, J. Bendix, J. Dreiser, *Chem. Sci.* **2014**, *5*, 1650–1660.
- [8] K. S. Pedersen, J. Dreiser, H. Weihe, R. Sibille, H. V. Johannesen, M. A. Sørensen, B. E. Nielsen, M. Sigrist, H. Mutka, S. Rols, J. Bendix, S. Piligkos, *Inorg. Chem.* **2015**, *54*, 7600–7606.
- [9] O. Waldmann, G. Carver, C. Dobe, D. Biner, A. Sieber, H. U. Güdel, H. Mutka, J. Ollivier, N. E. Chakov, *Appl. Phys. Lett.* **2006**, *88*, 042507.
- [10] D. H. Moseley, S. E. Stavretis, K. Thirunavukkuarasu, M. Ozerov, Y. Cheng, L. L. Daemen, J. Ludwig, Z. Lu, D. Smirnov, C. M. Brown, A. Pandey, A. J. Ramirez-Cuesta, A. C. Lamb, M. Atanasov, E. Bill, F. Neese, Z.-L. Xue, *Nat. Commun.* **2018**, *9*, 2572.

- [11] a) C. A. P. Goodwin, F. Ortu, D. Reta, N. F. Chilton, D. P. Mills, *Nature* **2017**, *548*, 439–442; b) A. Lunghi, F. Totti, S. Sanvito, R. Sessoli, *Chem. Sci.* **2017**, *8*, 6051–6059; c) L. Escalera-Moreno, N. Suaud, A. Gaita-Ariño, E. Coronado, *J. Phys. Chem. Lett.* **2017**, *8*, 1695–1700.
- [12] A. Furrer, J. Mesot, T. Strässle, *Neutron Scattering in Condensed Matter Physics*, World Scientific, Singapore, **2009**, pp. 12–13; A. Furrer, J. Mesot, T. Strässle, *Neutron Scattering in Condensed Matter Physics*, World Scientific, Singapore, **2009**, p. 17.
- [13] M. T. Dove, *Introduction to Lattice Dynamics*, Cambridge University Press, Cambridge, **1993**.
- [14] C. Fiolka, I. Pantenburg, G. Meyer, *Cryst. Growth Des.* **2011**, *11*, 5159–5165.
- [15] TOPAZ, website: <https://neutrons.ornl.gov/topaz>.
- [16] G. E. Bacon, *Neutron Scattering in Chemistry*, Butterworth, London, **1977**.
- [17] a) R. Basler, C. Boskovic, G. Chaboussant, H. U. Güdel, M. Murrie, S. T. Ochsnein, A. Sieber, *ChemPhysChem* **2003**, *4*, 910–926; b) S. E. Stavretis, M. Atanasov, A. A. Podlesnyak, S. C. Hunter, F. Neese, Z.-L. Xue, *Inorg. Chem.* **2015**, *54*, 9790–9801.
- [18] a) G. Ehlers, A. A. Podlesnyak, J. L. Niedziela, E. B. Iverson, P. E. Sokol, *Rev. Sci. Instrum.* **2011**, *82*, 085108; b) CNCS, website: <https://neutrons.ornl.gov/cnsc>; c) J. M. Carpenter, C. K. Loong, *Elements of Slow-Neutron Scattering: Basics, Techniques, and Applications*, Cambridge University Press, Cambridge, **2015**.
- [19] a) P. A. Seeger, L. L. Daemen, J. Z. Larese, *Nucl. Instrum. Methods Phys. Res. Sect. A* **2009**, *604*, 719–728; b) VISION, website: <https://neutrons.ornl.gov/vision>.
- [20] S. C. Hunter, A. A. Podlesnyak, Z.-L. Xue, *Inorg. Chem.* **2014**, *53*, 1955–1961.
- [21] a) P. W. M. Jacobs, *Group Theory with Applications in Chemical Physics*, Cambridge University Press, Cambridge, **2005**; b) C. Cohen-Tannoudji, B. Diu, F. Laloe, *Quantum Mechanics, Vol. 2*, Wiley, Chichester, **1977**, p. 1066; C. Cohen-Tannoudji, B. Diu, F. Laloe, *Quantum Mechanics, Vol. 2*, Wiley, Chichester, **1977**, p. 1313; c) F. A. Cotton, *Chemical Applications of Group Theory*, 3rd ed., Wiley, Chichester, **1990**, p. 303.
- [22] I. F. Silvera in *Far-Infrared Spectroscopy*, Wiley-Interscience, New York, **1971**, pp. 592–610.
- [23] J. R. Pilbrow, *J. Magn. Reson.* **1978**, *31*, 479–490.
- [24] C. Cohen-Tannoudji, F. Laloe, B. Diu, *Quantum Mechanics, Vol. 1*, Wiley, New York, **1977**, pp. 405–415.
- [25] Voigt geometry, see <https://www.ru.nl/hfml/facility/experimental/optical-experiments/>.
- [26] A. Togo, I. Tanaka, *Scr. Mater.* **2015**, *108*, 1–5.
- [27] a) B. S. Hudson, *Vib. Spectrosc.* **2006**, *42*, 25–32; b) B. S. Hudson in *Frontiers of Molecular Spectroscopy* (Ed.: J. Laane), Elsevier, Amsterdam, **2009**, pp. 597–622.
- [28] a) S. Gómez-Coca, A. Urtizberea, E. Cremades, P. J. Alonso, A. Camón, E. Ruiz, F. Luis, *Nat. Commun.* **2014**, *5*, 4300; b) W. H. Harman, T. D. Harris, D. E. Freedman, H. Fong, A. Chang, J. D. Rinehart, A. Ozarowski, M. T. Sougrati, F. Grandjean, G. J. Long, J. R. Long, C. J. Chang, *J. Am. Chem. Soc.* **2010**, *132*, 18115–18126; c) J. M. Zadrozny, M. Atanasov, A. M. Bryan, C.-Y. Lin, B. D. Rekker, P. P. Power, F. Neese, J. R. Long, *Chem. Sci.* **2013**, *4*, 125–138; d) J.-L. Liu, K. Yuan, J.-D. Leng, L. Ungur, W. Wernsdorfer, F.-S. Guo, L. F. Chibotaru, M.-L. Tong, *Inorg. Chem.* **2012**, *51*, 8538–8544; e) E. Lucaccini, L. Sorace, M. Perfetti, J.-P. Costes, R. Sessoli, *Chem. Commun.* **2014**, *50*, 1648–1651.
- [29] a) L. Chen, S.-Y. Chen, Y.-C. Sun, Y.-M. Guo, L. Yu, X.-T. Chen, Z. Wang, Z. W. Ouyang, Y. Song, Z.-L. Xue, *Dalton Trans.* **2015**, *44*, 11482–11490; b) S.-Y. Chen, H.-H. Cui, Y.-Q. Zhang, Z. Wang, Z.-W. Ouyang, L. Chen, X.-T. Chen, H. Yan, Z.-L. Xue, *Dalton Trans.* **2018**, *47*, 10162–10171.
- [30] R. L. Carlin, A. J. van Duynveldt, *Magnetic Properties of Transition Metal Compounds*, Springer, Berlin, **1977**.
- [31] a) K. N. Shrivastava, *Phys. Status Solidi B* **1983**, *117*, 437–458; b) A. Singh, K. N. Shrivastava, *Phys. Status Solidi B* **1979**, *95*, 273–277.
- [32] Y. Q. Cheng, L. L. Daemen, A. I. Kolesnikov, A. J. Ramirez-Cuesta, *J. Chem. Theory Comput.* **2019**, *15*, 1974–1982.

---

 Manuscript received: August 8, 2019

Accepted manuscript online: September 17, 2019

Version of record online: November 14, 2019